AIAA JOURNAL
Vol. 38, No. 10, October 2000

Jet Mixing Enhancement by High-Amplitude Fluidic Actuation

Jonathan B. Freund*
University of California, Los Angeles, Los Angeles, California 90095
and
Parviz Moin†
Stanford University, Stanford, California 94305

Recent experiments have shown that properly designed high-amplitude, low mass flux pulsed slot jets blowing normal to a jet's shear layer near the nozzle can significantly alter the jet's development. In contrast to commonly used low-amplitude forcing, this strong excitation appears to overwhelm the turbulence, having nearly the same effect at high and low Reynolds numbers. It can, therefore, be studied in detail by direct numerical simulation. Direct numerical simulations of Mach 0.9, Reynolds number 3.6×10^3 jets exhausting into quiescent fluid are conducted. Physically realistic slot jet actuators are included in the simulation by adding localized body-force terms to the governing equations. Three cases are considered in detail: a baseline unforced case and two cases that are forced with flapping modes at Strouhal numbers 0.2 and 0.4. ($Sr = 0.4$ was found to be the most amplified frequency in the unforced case.) Forcing at either frequency causes the jet to expand rapidly in the plane parallel with the actuators and to contract in the plane perpendicular to the actuators, as observed experimentally. It is found that the jet responds closer to the nozzle when forced at $Sr = 0.4$, but forcing at $Sr = 0.2$ is more effective at spreading the jet farther downstream. Several different measures of mixing (scalar dissipation, volume integrals of jet fluid mixture fraction, and point measurements of mixture fraction) are considered, and it is shown that by most, but not all, measures forcing at $Sr = 0.2$ is the more effective of the two at mixing.

Nomenclature

a = speed of sound
D = jet diameter
$\mathcal{D}$ = planar integral of $|\nabla\xi|$
e = total energy
$\mathcal{J}$ = volume integral of ξ^n
$\mathcal{M}$ = planar integral of ξ^n
r = radial coordinate
r_0 = jet nozzle radius
Sr = forcing Strouhal number, fD/U_j
T = temperature
U_a = peak actuator fluid velocity
U_j = jet exit velocity
v_r = radial velocity
v_x = axial velocity
v_θ = azimuthal velocity
x = axial coordinate
θ = azimuthal coordinate
ξ = jet fluid mixture fraction
ρ = fluid density
ω = vorticity magnitude

Introduction

THERE are several technological applications where enhanced jet mixing can lead to improved efficiency, reliability, or safety. For example, enhanced jet mixing can reduce temperatures on in-plume aerodynamic surfaces, such as the blown flap on a C-17 aircraft and thus provide greater flexibility in the choice of materials for their construction. Similarly, the mixing efficiency of fuel jets in combustors is an important factor in their overall performance, with size and weight reductions possible if mixing is improved. In the present work we focus on freejets, with the principal objective being plume temperature reduction.

In general, attempts to control jets can be divided into two categories: active and passive. Examples of passive control are tabs located at the nozzle exit,[1,2] crown-shaped nozzles,[3] and various other tailorings of the nozzle exit.[4–6] This list is far from exhaustive. Passive control is attractive because in many cases it entails only simple design modifications, a change in nozzle geometry, for example. Also its simplicity typically makes the resulting hardware less subject to failure. However, active control, where nozzle conditions are continuously updated, has greater flexibility and, therefore, greater potential to modify the jet flow. In this study we analyze a recently proposed method for active control of high-Reynolds-number jets.[7]

In the past, active excitation has been used extensively to understand the dynamics of free shear flows, particularly the dynamics of the largest turbulent flow structures. Studies up to the mid-1980s are summarized by Ho and Huerre,[8] and relatively more recent efforts are discussed by Parekh et al.[9] and Ho et al.[10] Here, the excitation used was typically low amplitude, often serving only to seed instability waves in the flow to phase correlate coherent structures. Unfortunately, it seems that to modify the flow significantly at high Reynolds numbers, low-amplitude forcing is ineffective because the applied perturbations are overwhelmed by the turbulence. Thus, control by low-amplitude excitation is not practical in many flows of engineering interest.

Recently, a scheme has been developed to control high-Reynolds-number jets, such as the exhaust flow from jet engines, by forcing with actuation velocities greater than the local turbulence intensity. This approach was tested by Parekh et al.,[7] who designed slot jets that blew normal to the jet shear layer adjacent to the nozzle (as in Fig. 1). When pulsed 180 deg out of phase from one another with peak blowing at approximately one-third the jet velocity (and approximately 2% of the jet mass flux), they excited large-scale oscillations in the jet that reduced the potential core length by over a factor of two. Recent test results have shown mixing enhancement using this technique on a full-scale engine.[11] Similar results have been obtained using zero net mass flux synthetic jets.[7,12,13] It appears that these active control approaches have been more successful at increasing mixing at high Reynolds numbers than any attempts by passive control approaches. Obviously, the direct numerical simulations used in this effort are incapable of addressing high-Reynolds-number flows, but we shall see that the behavior of

---

Received 13 September 1999; revision received 7 February 2000; accepted for publication 7 February 2000.

*Assistant Professor, Department of Mechanical and Aerospace Engineering; jfreund@seas.ucla.edu.

†Franklin and Caroline Johnson Professor of Mechanical Engineering, Department of Mechanical Engineering; also Senior Staff Scientist, NASA Ames Research Center, Moffett Field, CA 94035.

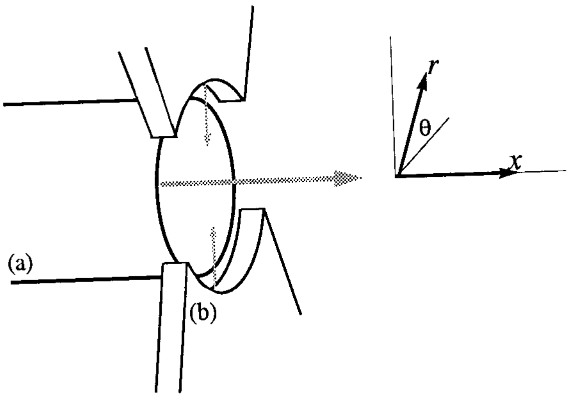

Fig. 1 Geometry schematic: a) jet nozzle and b) actuators.

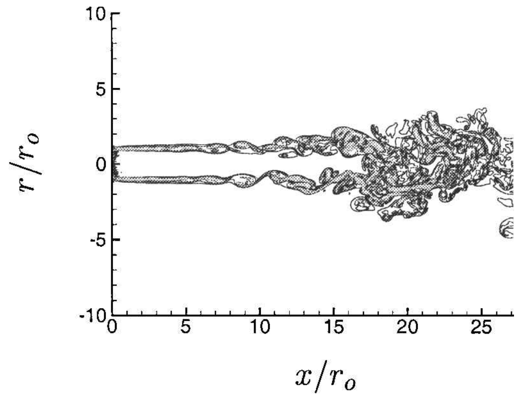

Fig. 2 Vorticity magnitude contours for the unforced case in an x–r plane; there are 40 evenly spaced contours with maximum $\omega r_0/U_j = 8.43$.

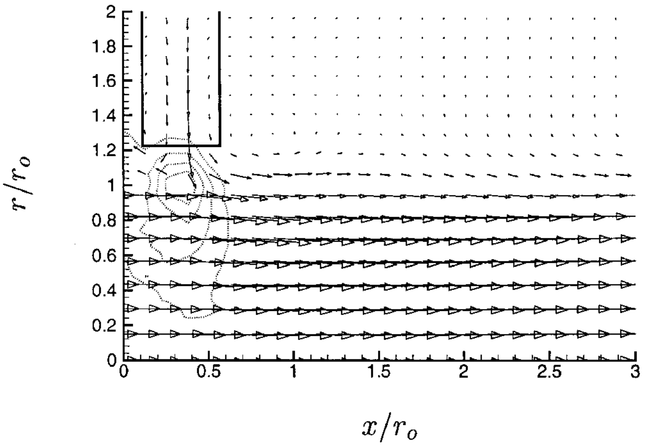

Fig. 3 Actuator flow impinging on the jet shear layer.

the simulated forced jets is similar to that observed at high Reynolds numbers, and new insights are provided.

Thus far, the forcing parameters in these experiments have been picked beforehand, as in an open-loop control strategy. Closed-loop control, where the jet flow would be continuously monitored and its state used to update the control parameters, may offer improved performance. To implement this approach a practical measure of the performance (an objective or cost function) is needed. An objective of the present effort is to study metrics for mixing and provide a database for direct comparison of different metrics. The choice of a metric for a particular application will depend not only on its relevance for the given mixing objective but also on practical aspects of its implementation. Here we concentrate only on the metrics themselves.

Flow Parameters

The focus of this paper is a round jet at Mach 0.9. The jet Reynolds number, based on centerline flow conditions at the nozzle exit, is 3.6×10^3, and the stagnation temperature of the jet is constant. These parameters match those studied experimentally by Stromberg et al.,[14] and a baseline, unforced case has been validated against their data.[15] Direct comparison shows that mean Mach number profiles (and the overall sound pressure levels on an arc at 60 radii from the nozzle) agree to within 5%. Unfortunately, the precise nozzle conditions were not measured, but spectra show that the initial jet shear layers were laminar, as expected at this Reynolds number. To model appropriate nozzle conditions, a rounded top-hat velocity profile was specified in the present simulations (see the Appendix). Small-amplitude ($v' < 0.01U_j$) random velocity fluctuations were added to this to seed the turbulence. The consequence of not adding random perturbations was a prolonged region of laminar flow near the nozzle, but the flow downstream was not particularly sensitive to the nature of these disturbances provided that they contained a range of frequencies and wave numbers.

Slot jets shown in Fig. 1 were used to excite the flow in a manner similar to the experiments of Parekh et al.[7] Each slot extended 90 deg around the jet and blew normal to the shear layer just downstream of the nozzle. The techniques for including these actuators in the simulations and their exact specifications are outlined with the numerical method in the Appendix. The individual slot jets blew 180 deg out of phase from one another to excite a flapping mode in the jet, and their velocity varied sinusoidally between 0 and $0.6U_j$. The net mass flow fraction of the actuators was $\dot{M}_{\rm act}/\dot{M}_{\rm jet} \approx 0.035$. Two forced jets where computed. The first was forced at Strouhal number $Sr = 0.2$, which had been found experimentally to be very effective at spreading the jet.[7] The other case was forced at $Sr = 0.4$, which was the most amplified frequency of the unforced jet, as found both by the simulations and the cited experiment.[14]

Results

Visualizations

Figure 2 shows a vorticity magnitude visualization of the unforced case. The initial jet shear layers are seen to be laminar. By $x = 5r_0$, instability waves appear that develop into Kelvin–Helmholtz rollers by $x = 10r_0$. Their passing frequency is $Sr = 0.4$, in accord with the experiments of Stromberg et al.,[14] who found in their facility that $Sr = 0.44$ was the peak Strouhal number in the early development of their jet, subject to ±10% day-to-day variation. At the instant shown, the potential core extends to approximately $x = 17r_0$. Near the end of the potential core a transition to turbulence occurs, which is corroborated by Reynolds stress statistics that will be reported elsewhere.[15]

Figure 3 shows a close-up of an actuator near its peak blowing condition. (The $Sr = 0.2$ case is shown, but the $Sr = 0.4$ case is similar.) There were only eight mesh points across the modeled actuator in the streamwise direction, and those near the center of the actuator, where the Gaussian axial velocity distribution peaks (see the Appendix), carry most of the momentum flux. Every other mesh point in x and every sixth mesh point in r is shown. The solid rectangle indicated the extent of the actuator. Light contours show $(p - p_\infty)/\rho_j U_j^2$ at evenly spaced intervals (minimum $= 0.0333$, maximum $= 0.133$). A region of increased pressure just below the actuator is also shown with contours in Fig. 3. The initial effect of the forcing on the jet is seen just downstream of the actuator where the primary jet flow is slightly deflected. The bulk of the fluid exiting the actuator appears to be turned downstream as it encounters the jet; however, a portion of it is also turned upstream, giving the appearance of a stagnation point flow. The pressure rise in this region is also reminiscent of a stagnation point flow.

The result of the forcing downstream is visualized in Figs. 4 and 5 for the $Sr = 0.2$ and 0.4 cases, respectively. In Figs. 4 and 5, 20 evenly spaced contours between $\omega r_0/U_j = 0.6$ and 12.0 are shown. It is clear for the $Sr = 0.2$ case that the actuators excite the jet significantly and that it spreads rapidly in the $\theta = \pi/2$ plane. In the $\theta = 0$ plane, the spreading is suppressed. A single mode appears to dominate the early development of the jet as evidenced by the large structures visible before $x = 10r_0$. The instantaneous visualization in Fig. 4 shows the potential core closing at approximately $x = 9r_0$. Downstream of this region, the vorticity magnitude field shows an eruption

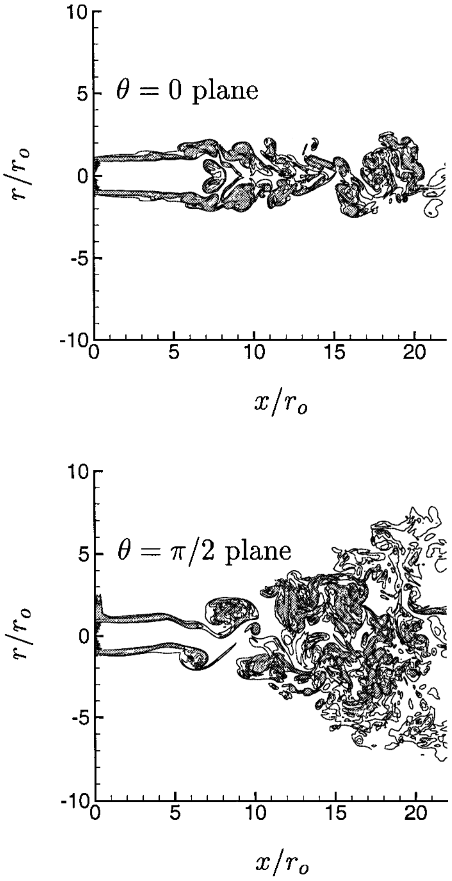

Fig. 4 Vorticity magnitude contours for the case forced at $Sr = 0.2$.

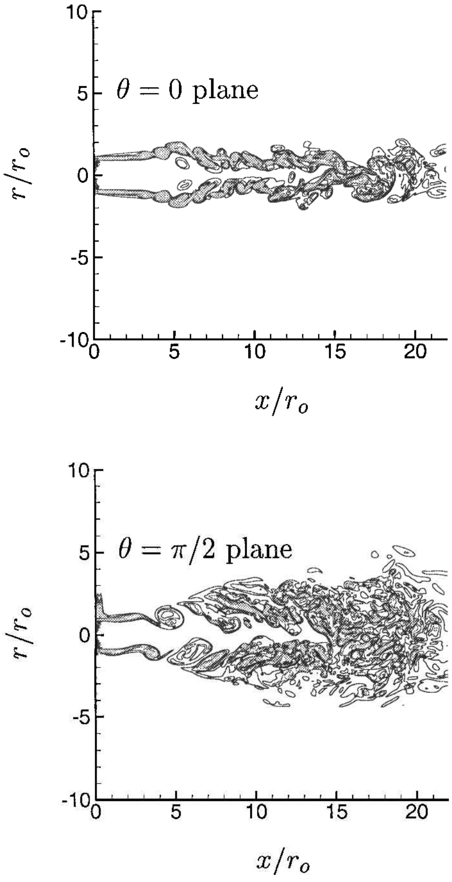

Fig. 5 Vorticity magnitude contours for the case forced at $Sr = 0.4$.

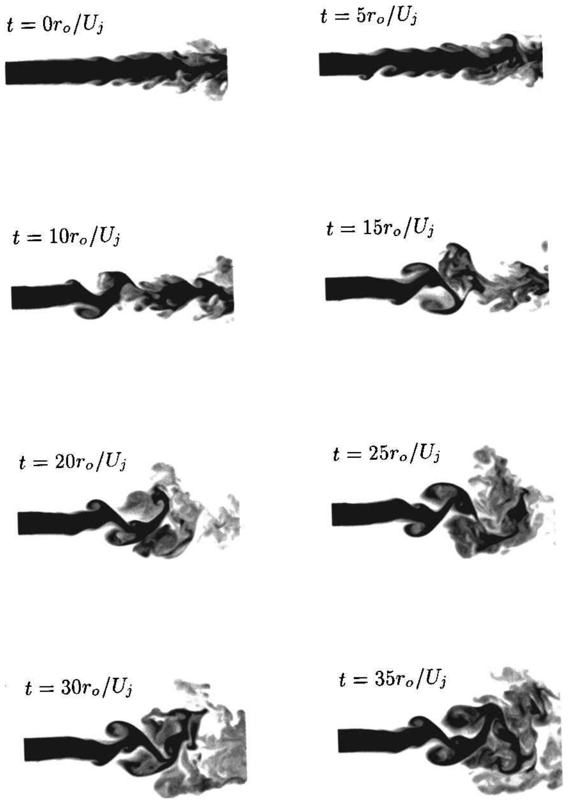

Fig. 6 Development of the scalar field in the $\theta = \pi/2$ plane once $Sr = 0.2$ forcing is turned on at $t = 0$.

of small-scale turbulence. A surprising feature of the visualization is the apparent symmetry near $x = 7r_0$ in the $\theta = 0$ plane. This is the characteristic feature of the large-scale coherent structures seen in the $\theta = \pi/2$ visualization as they intersect the $\theta = 0$ plane.

When the jet is forced at $Sr = 0.4$ (Fig. 5), the large-scale structures are smaller but appear earlier, which is not surprising because this is the most amplified frequency in the unforced jet. However, the downstream effect of the forcing is now quite different. The structures disappear or are obscured by small scales almost immediately, and the jet spreads less in the plane of the actuators ($\theta = \pi/2$). Though the shear layers appear thicker early in the development, they slow their spreading and merge only at around $x = 13r_0$, beyond where they merge in the $Sr = 0.2$ case. The visualization in the $\theta = 0$ plane is similar to the $Sr = 0.2$ case, with similar symmetries at small x due to the coherence of the excited structures, but a longer potential core.

Figure 6 shows a series of instantaneous visualizations of the jet fluid mixture fraction as it adjusts to forcing at $Sr = 0.2$ (black is pure jet fluid and white is pure ambient fluid). The time series starts from the unforced jet and the actuators turn on at $t = 0$. By $t = 10r_0/U_j$, there is clear evidence of large coherent structures distorting the scalar field. As expected, these travel at approximately $0.65U_j$, appearing at $x \approx 10r_0$, the horizontal midpoint of the region shown, at $t \approx 15r_0/U_j$. The scalar field takes considerably longer to develop farther downstream where decreasing velocities slow advection. For computing statistics, the forced jets were assumed to be fully developed only after $t = 80r_0/U_j$. The simulations were run to approximately $t = 150r_0/U_j$.

Figure 7 shows the corresponding set of images for the jet forced at $Sr = 0.4$. Again we see that at this forcing frequency, large structures appear closer to the nozzle than in the $Sr = 0.2$ case. The mixed regions in the jet shear layers thicken rapidly, but a tongue of pure fluid persists along the domain centerline. The flapping of the jet column is also less pronounced.

Mean Flow

Mean axial velocity $\bar{v}_x$ provides a more quantitative measure of the effect of the forcing on the jet development. Approximately 700

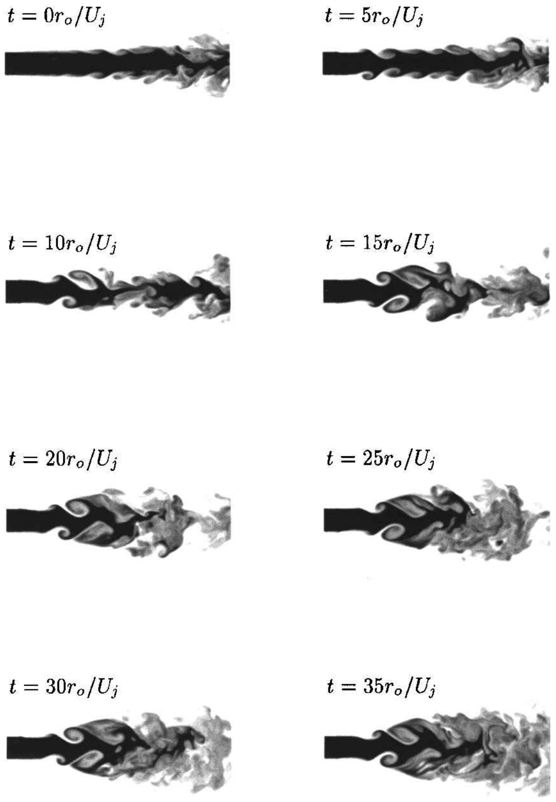

Fig. 7 Development of the scalar field in the $\theta = \pi/2$ plane once $Sr = 0.4$ forcing is turned on at $t = 0$.

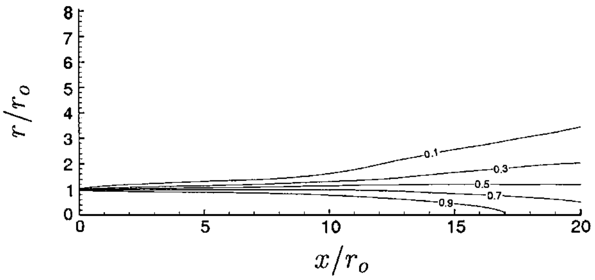

Fig. 8 Mean axial velocity ($\bar{v}_x/U_j$) for the unforced jet.

fields spaced in time by $\Delta T_{\mathrm{av}} = 0.2r_0/U_j$ were averaged to compute the mean. Symmetries were exploited to increase the statistical sample. We see that the jet spreads as expected (Fig. 8), first slowly where the shear layers are laminar and then more quickly near the end of the potential core where the flow goes through transition. If $\bar{v}_x/U_j = 0.9$ is used to designate the end of the potential core, in this case the potential core closes at $x = 17r_0$, which is farther downstream than would be expected for high-Reynolds-number jets, because the shear layers are initially laminar and, therefore, spread slowly.

Forcing at $Sr = 0.2$ dramatically alters the mean flow (Fig. 9). In the plane perpendicular to the action of the actuators ($\theta = 0$) the jet at first spreads more rapidly than the unforced case, but then this is reversed starting at the end of the potential core ($x = 8r_0$). Only near $x = 20r_0$ does the 10% velocity contour extend to the same radial distance as at $x = 8r_0$. The contours have an unusual thumb shape at $r = r_0$, $x = 8r_0$ that is caused by the large-scale structures seen in Fig. 4. Based on visualizations, (for example, Fig. 4), these structures first intersect the $\theta = 0$ plane near $r = 0$, and thus, they bring lower velocity fluid into that region before the region near $r = r_0$. Therefore, at this downstream location, the velocity is higher near $r = r_0$, which causes the appearance of the thumb. In the $\theta = \pi/2$ plane, the jet is seen to spread rapidly starting near $x = 8r_0$, and this continues until the end of the computational domain at $x = 20r_0$. Parekh et al.[7] showed very similar results for forcing at this same frequency.

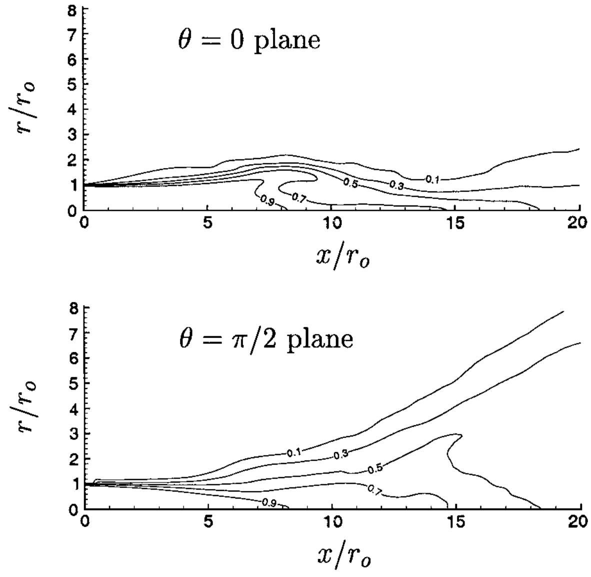

Fig. 9 Mean axial velocity ($\bar{v}_x/U_j$) for $Sr = 0.2$ forcing.

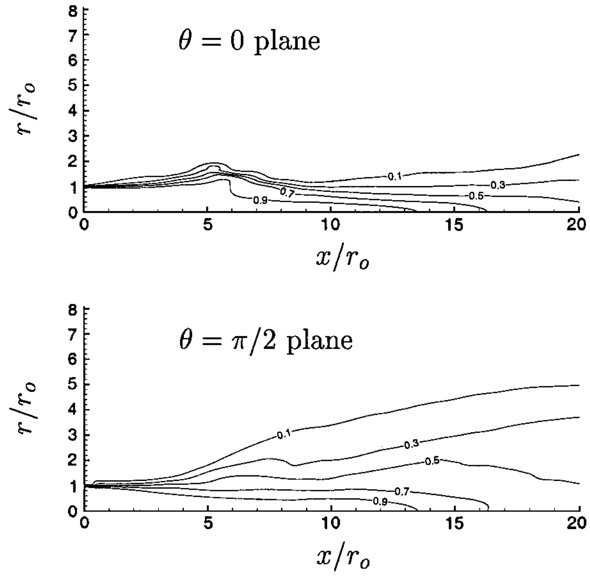

Fig. 10 Mean axial velocity ($\bar{v}_x/U_j$) for $Sr = 0.4$ forcing.

When the jet is forced at $Sr = 0.4$ (Fig. 10), the mean flow is markedly different. In the $\theta = 0$ plane, the jet spreads only until around $x = 5.5r_0$ before spreading is reversed. It does this significantly closer to the nozzle than in the $Sr = 0.2$ case. There is again an unusual shape to the contours at this point, but at this forcing frequency it is less pronounced. Though spreading in the $\theta = 0$ plane is reversed at smaller x than it was for $Sr = 0.2$ forcing, the potential core is now longer, extending to $x = 13.5r_0$. In the $\theta = \pi/2$ plane, the jet spreads rapidly starting at around $5.5r_0$, but spreading slows downstream, and the jet does not grow as much radially as in the $Sr = 0.2$ case (Fig. 9).

Unsteady Response of the Jet

To optimize the forcing, by either an open- or closed-loop approach, it is necessary to develop a measure of its effectiveness. Naturally, the choice of a definition for mixing effectiveness will depend on the specific objective of the application. Here we will consider several metrics that are of potential use in temperature abatement or combustion applications.

Point Measurements of ξ

We first consider point measures of jet fluid mixture fraction ($\xi = 1$ for pure jet fluid and $\xi = 0$ for pure ambient fluid) on the

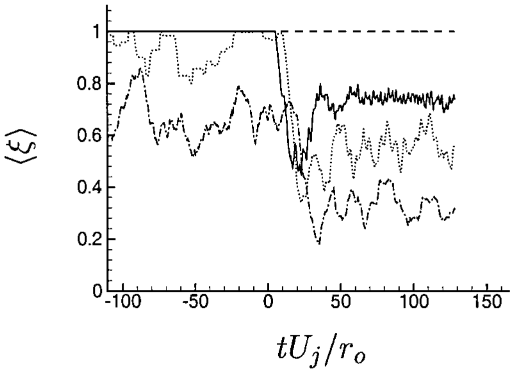

a) $Sr = 0.2$

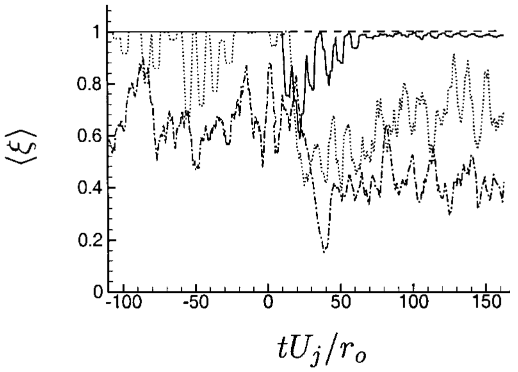

b) $Sr = 0.4$

Fig. 11 Time histories of scalar on the jet axis: ----, $x = 5r_0$; ——, $x = 10r_0$; ...., $x = 15r_0$; and – -, $x = 20r_0$.

jet axis. If the jet were hot, the concentration of jet fluid (mixture fraction) would closely correspond to temperature. Extensive centerline measurements have been made in forced jets and have been used to estimate the mixing enhancement of various forcings.[7] Figure 11 shows time histories of $\langle\xi\rangle$ on the jet axis ($r = 0$) and at $x = 5$, 10, 15, and $20r_0$. The angle braces $\langle\ \rangle$ indicate an average over a single period of the forcing: $T_a = 9.9r_0/U_j$ for $Sr = 0.2$ and $T_a = 4.9r_0/U_j$ for $Sr = 0.4$. Despite this average, there is still considerable oscillation in the measure due to the chaotic nature of turbulence. Averaging for longer periods would, of course, smooth the profiles, but for closed-loop control applications it is important to be able to measure quickly the response of the jet to changes in the forcing. Longer averages would slow the response of the metric to the changes in the forcing.

We see in Fig. 11 that, before forcing is initiated at $t = 0$, the flow is pure jet fluid at $x = 5r_0$ and $x = 10r_0$. At $x = 15r_0$, there is slight mixing with ambient fluid, and at $x = 20$, the mixture fraction hovers around its long-time (if forcing were not initiated) mean $\bar{\xi} = 0.65$. As expected from observations of the potential core length, the mixture fraction at $x = 5r_0$ is unaffected by the forcing at either Strouhal number. At $Sr = 0.2$ (Fig. 11a), the mixture fraction at $x = 10r_0$ is the first to respond to the forcing. It initially decreases to $\langle\xi\rangle = 0.5$, but rises again and remains near the mean $\bar{\xi} = 0.75$ for $t > 60r_0/U_j$. The period-averaged values at $x = 15r_0$ and $20r_0$ also seem to overshoot initially before they settle to hover around their apparent long-time mean values of $\bar{\xi} = 0.6$ and 0.3, respectively. The small statistical sample size makes these values and the point where they are reached somewhat imprecise. Forcing at $Sr = 0.4$ also causes a greater reduction in centerline mixture fraction initially (Fig. 11b). The curve at $x = 10r_0$ initially dips, but recovers to nearly its unforced, pure jet fluid level by $t = 70r_0/U_j$. The curves at $x = 15r_0$ and $20r_0$ hover around their mean values of $\bar{\xi} = 0.7$ and 0.4. It is unclear why this case takes longer to equilibrate than the lower frequency forcing.

The initial overreaction of the jet to the forcing can be explained qualitatively with a simple model where the large-scale structures are assumed to be linear instability waves. Given this model, turbulent structures will grow, stabilize, and decay as the layer spreads. If the jet spreads slowly, as in the unforced case, there is a long region of growth before decay. Thus, given a significant initial forcing amplitude, the structures can become quite intense by a linear mechanism. However, high-amplitude disturbances will also increase the spreading rate of the layer and thereby reduce the distance over which subsequent disturbances can amplify. Hence, by this model, the first forced structure sees a slowly spreading layer and, thus, can grow more than subsequent disturbances that see a more rapidly spreading layer, which explains the observed overshoot.

This model can also explain the greater response of the jet to $Sr = 0.2$ forcing than forcing at its natural frequency $Sr = 0.4$. Instability analysis shows that, for thicker shear layers, as would be present in forced jets, the most amplified instability waves will have a longer wavelength and lower frequency.[16] Therefore, it is not surprising that $Sr = 0.2$ is more successful. Unfortunately, linear stability predictions can only loosely model the quantitative behavior of turbulence. An accurate quantitative prediction using linear stability analysis is, therefore, not likely to be successful in conjunction with the high-amplitude forcing used in the present study.

Volume Integrals of ξ^n

Volume integrals of ξ^n can also provide a measure of mixing effectiveness. For $n \approx 4$–6 this will provide a crude model, assuming $\xi \propto T$, of the infrared signature of the jet. Time histories of

$$\mathcal{J} = \int_{\Omega_c} \xi^n \, \mathrm{d}V \qquad (1)$$

where Ω_c is the physical domain ($x < 20r_0$, $r < 10r_0$), are shown in Fig. 12. No time averaging was necessary to smooth curves in this case. We see that the volume integrals of ξ^1 and ξ^2 both increase when the jet is forced. For both cases, the ξ^1 curve shows that there is 60% more jet fluid in the domain. Despite this increase, ξ^4 and ξ^6 decrease, thus indicating improved mixing. The ξ^6 curve decreases from its unforced value $\mathcal{J}_0$ to $\mathcal{J} = 0.7\mathcal{J}_0$ for the $Sr = 0.2$ case and $\mathcal{J} = 0.6\mathcal{J}_0$ for the $Sr = 0.4$ case. It is somewhat surprising that the $Sr = 0.4$ case shows better mixing by this measure because the opposite was predicted based on centerline measurements (Fig. 11). It may also seem counter to the visualizations and mean flow data, which show greater spreading for $Sr = 0.2$ forcing. Because Eq. (1) depends on the axial dimension of the computational box, it is,

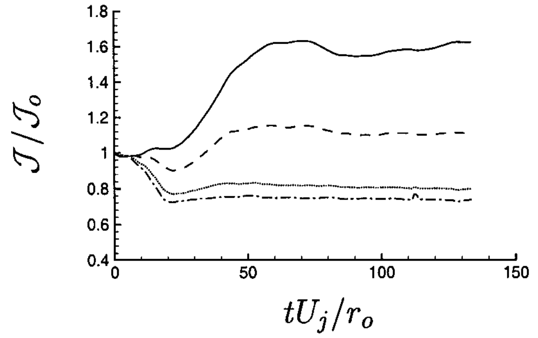

$Sr = 0.2$ forcing

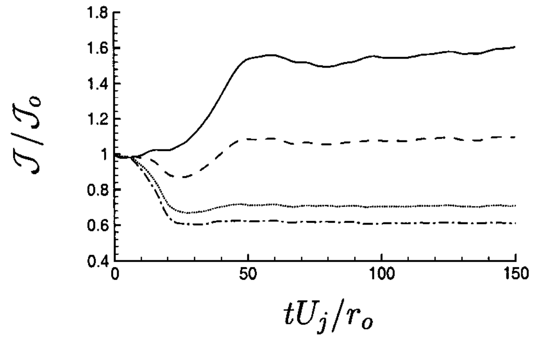

$Sr = 0.4$ forcing

Fig. 12 Integrals of ξ^n with: ——, $n = 1$; ----, $n = 2$; ...., $n = 4$; and – -, $n = 6$.

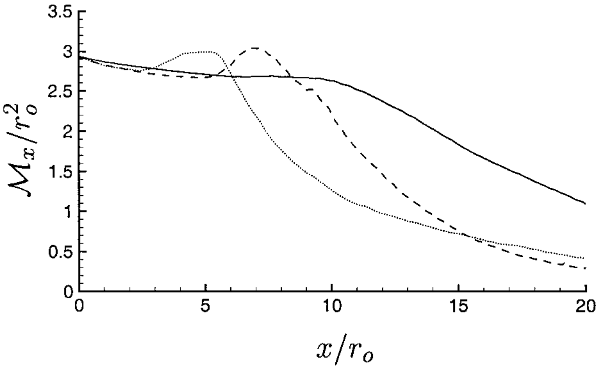

Fig. 13 Planar integrals of ξ^6 from Eq. (2): ——, unforced; - - - -, $Sr = 0.2$; and . . . . , $Sr = 0.4$.

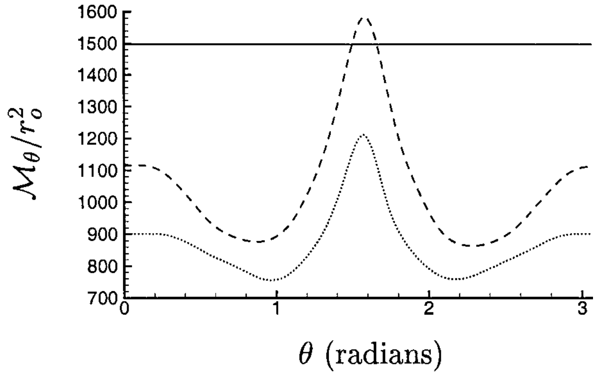

Fig. 14 Planar integrals of ξ^6 from Eq. (3): ——, unforced; - - - -, $Sr = 0.2$; and . . . . , $Sr = 0.4$.

therefore, important to also estimate downstream mixing based on the available data. (Note that the finite radial dimension does not affect the result because $\xi \rightarrow 0$ by $r = 10r_0$, the radial box size.)

We can make such an extrapolation by computing mixedness as a function of downstream distance. Figure 13 shows the planar contributions to $\mathcal{J}$ as a function of x for $t > 80r_0/U_j$:

$$\mathcal{M}_x(x) = \int_0^{2\pi}\int_0^{10r_0} \xi^6 r \,\mathrm{d}r\,\mathrm{d}\theta \tag{2}$$

It now becomes clear that the apparent advantage of $Sr = 0.4$ forcing is primarily a result of the jet's more rapid response to the forcing. At the outflow boundary we see that the $Sr = 0.2$ forced jet is actually mixed better (by this measure) and $\mathcal{M}_x$ has a steeper slope (rate of mixing) than the jet forced at $Sr = 0.4$. Though it is not possible to make firm judgments about the subsequent downstream mixing, based on the level and slope of $\mathcal{M}_x$ at $x = 20r_0$ it appears that the $Sr = 0.2$ case might be better if more downstream fluid could be included in Eq. (1). Both forced cases are clearly better than the unforced case, also shown in Fig. 13.

The asymmetry of the jets is seen in Fig. 14, which shows planar integrals of ξ^6 at constant θ,

$$\mathcal{M}_\theta(\theta) = \int_{-20r_0}^{20r_0}\int_0^{10r_0} \xi^6 \,\mathrm{d}r\,\mathrm{d}x \tag{3}$$

For both forced cases, this metric peaks in the $\theta = \pi/2$ plane, the plane of the actuators. For both Strouhal numbers, this peak is roughly 1.75 times as high as the minimum values. Somewhat surprisingly these minima do not occur at $\theta = 0$ (Fig. 14), which is perpendicular to the actuators. $\mathcal{M}_\theta$ is 20% higher at $\theta = 0$ than at its minima. Nearly everywhere $\mathcal{M}_\theta$ is suppressed below its value in the unforced case, more so in the $Sr = 0.4$ case. Note that the details of these results also depend on the box size. Because the forced jets are still highly asymmetric at the outflow boundary, the numerical differences between the peaks in valley would increase if more downstream data were available.

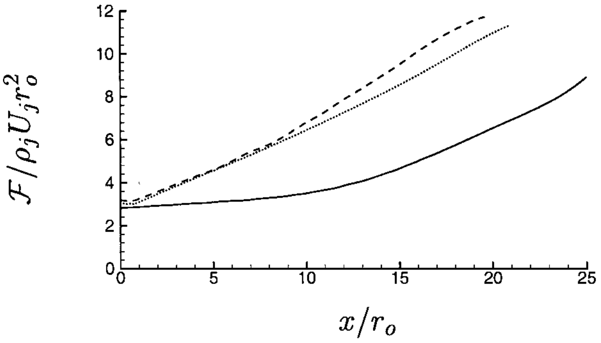

Fig. 15 Streamwise mass flux from Eq. (4): ——, unforced; - - - -, $Sr = 0.2$; and . . . . , $Sr = 0.4$.

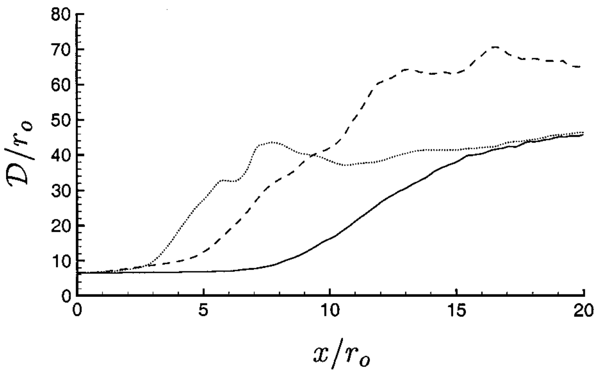

Fig. 16 Planar integrals of $|\nabla\xi|$ from Eq. (5): ——, unforced; - - - -, $Sr = 0.2$; and . . . . , $Sr = 0.4$.

Streamwise Mass Flux

The net entrainment of the jet can be studied by computing the streamwise mass flux. Because v_x is negligible at $r = 10r_0$, this is equivalent to

$$\mathcal{F}(x) = \int_0^{2\pi}\int_0^{10r_0} \overline{\rho v_x} r \,\mathrm{d}r\,\mathrm{d}\theta \tag{4}$$

which is plotted in Fig. 15. The mass flux in the unforced case grows slowly at first, where the shear layers are laminar and disturbances are small, and then grows more rapidly starting at around $x = 14r_0$, where the potential core closes. The mass fluxes in the forced cases both grow rapidly from the start and are over twice as high by $x = 20r_0$. Forcing at $Sr = 0.2$ is only mildly more effective at increasing the mass flux than forcing at $Sr = 0.4$. It is seen that the fluxes are slightly different for the three cases at $x = 0$. This is because of the fluid added by the actuators and entrainment caused directly by their action.

Scalar Dissipation

The rate of scalar dissipation can also provide an important measure of mixing that is particularly relevant in combustion applications. In Fig. 16, we consider planar integrals of $|\nabla\xi|$ as a function of downstream distance,

$$\mathcal{D}(x) = \int_0^{2\pi}\int_0^{10r_0} |\nabla\xi| r \,\mathrm{d}r\,\mathrm{d}\theta \tag{5}$$

$\mathcal{D}(x)$ for the $Sr = 0.4$ case starts to rise closer to the nozzle, but the curve for $Sr = 0.2$ forcing follows only $2r_0$ farther downstream and becomes 50% greater by the right side of the domain. The total dissipation in the computational domain is clearly larger for $Sr = 0.2$ forcing. Based on the data at $x = 20r_0$, this trend is likely to continue downstream.

Summary

Simulations of jets forced with high-amplitude actuation reproduced experimental observations of similarly forced jets. Visualizations showed the dramatic effect of this forcing on the jet. Forcing at

$Sr = 0.2$ excited the jet column into a distinct flapping mode. When forced at $Sr = 0.4$, the most amplified frequency in the unforced jet, the large structures appeared closer to the nozzle. However, despite the rapid initial spreading of this jet, forcing at $Sr = 0.4$ was not as effective at spreading the jet and mixing it (by most measures) with the ambient flow downstream. Mean axial velocities showed that the jet becomes highly nonaxisymmetric in both forced cases and that the potential core length was reduced more by $Sr = 0.2$ than $Sr = 0.4$ forcing.

Mixing was quantified by several different metrics. Point measurements of scalar concentration on the jet axis showed that forcing at $Sr = 0.2$ was more effective at reducing centerline scalar concentration. However, volume integrals of ξ^n over the computational domain (for $n = 4$ or 6) were smaller when the jet was forced with $Sr = 0.4$. This was primarily due to the faster response of the jet to forcing at this frequency. Consideration of planar integrals of ξ^6 and $|\nabla\xi|$ as a function of x suggested that forcing at $Sr = 0.2$ would be more effective for mixing farther downstream. Forcing at both Strouhal numbers increased streamwise mass flux considerably over the unforced case, with $Sr = 0.2$ forcing performing marginally better in this regard than $Sr = 0.4$ forcing.

Appendix: Simulation Techniques

The full compressible Navier–Stokes equations and an advection–diffusion equation were solved in cylindrical coordinates without modeling assumptions. Full details of the basic numerical algorithm are given by Freund et al.,[17] where the same algorithm was used to study turbulence in compressible mixing layers. Only a summary of the method is provided here. Sixth-order compact finite differences[18] were used to compute derivatives in the streamwise x and radial r directions, and Fourier spectral methods were used in the azimuthal direction θ. A fourth-order Runge–Kutta algorithm was used to advance the solution in time. At the $r = 0$ coordinate singularity, the equations were solved in Cartesian coordinates. To maintain a reasonable numerical time step given the restriction imposed by the Runge–Kutta algorithm, higher Fourier modes in θ were not used near $r = 0$. They were omitted systematically so that the effective azimuthal resolution remained nearly constant with radial location. The computational mesh had $440 \times 230 \times 160$ points in the axial, radial, and azimuthal directions, respectively. Mesh points were compressed in the radial direction around $r = r_0$.

The boundary conditions, the jet nozzle, and the actuators were all accounted for by modifying the equations in appropriate regions of the computational domain. The rest of the computational domain that is free of these terms is referred to as the physical domain. The artificial terms serve to model an infinite domain, the nozzle, or the actuators where needed. For example, non-reflecting outflow and lateral (large r) boundary conditions were approximated by stretching the mesh beyond the physical domain and filtering the solution on that stretched mesh. A typical mesh is shown in Fig. A1. Similar boundary conditions have been used in aeroacoustic computations, and additional documentation is available elsewhere.[15,19]

In a zone of width r_0 at the inflow side of the computational domain (Fig. A1), terms were added to the equations that drive the solution toward the desired nozzle conditions. If the compressible flow equations are represented by $N(\boldsymbol{q}) = 0$, where $\boldsymbol{q}$ is a vector of flow quantities, then the modified equation has the form $N(\boldsymbol{q}) = -\sigma(\boldsymbol{q} - \boldsymbol{q}_{\text{target}})$, where $\boldsymbol{q}_{\text{target}}$ is the desired nozzle conditions. The added term acts like a penalty function. The value of σ in this zone was $2.5a_\infty / r_0$, and the target axial velocity was a typical hyperbolic tangent top-hat profile:

$$\frac{\bar{v}_{x_{\text{target}}}}{U_j} = \frac{1}{2}\left\{1 - \tanh\left[12.5\left(\frac{r}{r_0} - \frac{r_0}{r}\right)\right]\right\} \tag{A1}$$

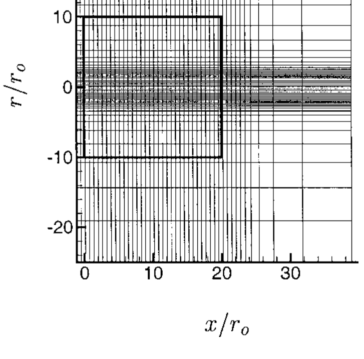

Fig. A1 Mesh showing every tenth mesh point for the forced jet simulations; thick rectangle demarks the physical portion of the computational domain.

The density and scalar profiles were similarly specified. Random velocity fluctuations where added to this mean profile using a similar body-force method. This randomization was low amplitude ($v' < 0.01U_j$) and served only to seed the turbulence with broadbanded noise.

The actuators were included by similar body-force methods. The actuators extended axially from $x_1 = 0.13r_0$ to $x_2 = 0.57r_0$ (8 mesh points) and radially from $r_1 = 1.11r_0$ to $r_2 = 3.5r_0$ (101 mesh points). In this region, $\sigma = 2.5a_\infty / r_0$ and $\boldsymbol{q}_{\text{target}} = [\rho, \rho v_x, \rho v_r, \rho v_\theta, e, \rho\xi]^T_{\text{target}} = [0.75\rho_\infty, 0, -0.75\rho_\infty v_a, 0, e_a, 0]^T$ with e_a calculated from $\rho = 0.75\rho_\infty$, v_a, and the ambient pressure. The instantaneous actuator target velocity was

$$v_a = U_a f_x(x) f_r(r) f_\theta(\theta) f_t(t) \tag{A2}$$

Its amplitude was set at $U_a = U_j$, but the actual peak v_r at the actuator only reached $0.6U_j$ because the body forcing was resisted by viscosity. The spatial and temporal dependencies of v_a were

$$f_x(x) = \exp\left\{-\alpha_x[x - 0.5(x_1 + x_2)]^2\right\} \tag{A3}$$

$$f_r(r) = \exp\left[-\alpha_r(r - r_1)^2\right] \tag{A4}$$

$$f_\theta(\theta) = \exp\left[-\zeta(\theta)^{8e^{-\zeta(\theta)^2} + 2.8}\right] + \exp\left\{-[\zeta(\theta) - 4]^{8e^{-[\zeta(\theta) - 4]^2} + 2.8}\right\} \tag{A5}$$

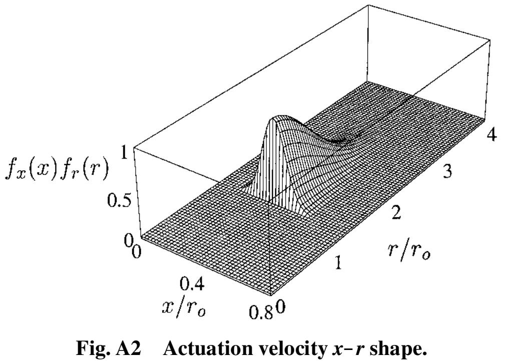

Fig. A2 Actuation velocity x–r shape.

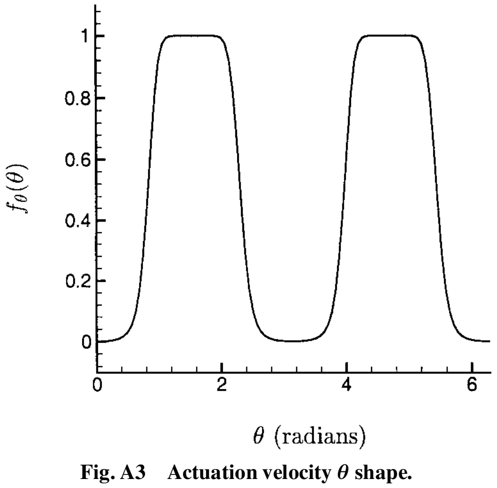

Fig. A3 Actuation velocity θ shape.

$$f_t(t) = 0.5\left[1 + \sin(2\pi St U_j t / D)\operatorname{sgn}(\sin\theta)\right] \qquad (A6)$$

where $\alpha_x = 95.1$, $\alpha_r = 1.34$, and $\zeta(\theta) = 8\theta/2\pi - 2$. The x–r shape of v_a is plotted in Fig. A2, and the azimuthal dependence is plotted in Fig. A3. The sgn term in Eq. (A6) makes the actuators act out of phase.

Acknowledgments

This work was supported by the Air Force Office of Scientific Research. The authors thank David Parekh and Alan Cain for many useful discussions on jet mixing, particularly with regard to the cited experimental studies.

References

[1] Samimy, M., Zaman, K. B. M. Q., and Reeder, M. F., "Effect of Tabs on the Flow and Noise Field of an Axisymmetric Jet," *AIAA Journal*, Vol. 31, No. 4, 1993, pp. 609–619.

[2] Reeder, M. F., and Samimy, M., "The Evolution of a Jet with Vortex Generating Tabs: Real-Time Visualization and Quantitative Measurements," *Journal of Fluid Mechanics*, Vol. 311, March 1996, pp. 73–118.

[3] Longmire, E. K., Eaton, J. K., and Elkins, C. J., "Control of Jet Structure by Crown-Shaped Nozzles," *AIAA Journal*, Vol. 30, No. 2, 1992, pp. 505–512.

[4] Wlezien, R. W., and Kibens, V., "Influence of Nozzle Asymmetry on Supersonic Jets," *AIAA Journal*, Vol. 26, No. 1, 1988, pp. 27–33.

[5] Krothapalli, A., McDaniel, J., and Baganoff, D., "Effect of Slotting on the Noise of an Axisymmetric Supersonic Jet," *AIAA Journal*, Vol. 28, No. 12, 1990, pp. 2136–2144.

[6] Zaman, K. M. B. Q., "Spreading Characteristics of Compressible Jets from Nozzles of Various Geometries," *Journal of Fluid Mechanics*, Vol. 383, March 1999, pp. 197–228.

[7] Parekh, D. E., Kibens, V., Glezer, A., Wiltse, J. M., and Smith, D. M., "Innovative Jet Flow Control: Mixing Enhancement Experiments," AIAA Paper 96-0308, 1996.

[8] Ho, C.-M., and Huerre, P., "Perturbed Free Shear Layers," *Annual Review of Fluid Mechanics*, Vol. 16, 1984, pp. 365–424.

[9] Parekh, D. E., Reynolds, W. C., and Mungal, M. G., "Bifurcation of Round Air Jets by Dual-Mode Acoustic Excitation," AIAA Paper 87-1064, 1987.

[10] Ho, C.-M., Zohar, Y., Foss, J. K., and Buell, J. C., "Phase Decorrelation of Coherent Structures in a Free Shear Layer," *Journal of Fluid Mechanics*, Vol. 230, Sept. 1991, pp. 319–337.

[11] McKinney, G., "Research Highlights," Air Force Office of Scientific Research Communication and Technical Information, Arlington, VA, Sept./Oct. 1998.

[12] Smith, B. L., and Glezer, A., "The Formation and Evolution of Synthetic Jets," *Physics of Fluids*, Vol. 10, No. 9, 1998, pp. 2281–2297.

[13] Smith, B. L., and Glezer, A., "Vectoring and Small-Scale Motions Effected in Free Shear Flows Using Synthetic FET Actuators," AIAA Paper 97-0213, 1997.

[14] Stromberg, J. L., McLaughlin, D. K., and Troutt, T. R., "Flow Field and Acoustic Properties of a Mach Number 0.9 Jet at a Low Reynolds Number," *Journal of Sound and Vibration*, Vol. 72, No. 2, 1980, pp. 159–176.

[15] Freund, J. B., "Noise Sources in a Low Reynolds Number Turbulent Jet at Mach 0.9," *Journal of Fluid Mechanics* (submitted for publication).

[16] Michalke, A., "A Survey on Jet Instability Theory," *Progress in Aerospace Sciences*, Vol. 21, 1984, pp. 159–199.

[17] Freund, J. B., Moin, P., and Lele, S. K., "Compressibility Effects in a Turbulent Annular Mixing Layer," Mechanical Engineering, Flow Physics and Computation Div., TR TF-72, Stanford Univ., Stanford, CA, Sept. 1997.

[18] Lele, S. K., "Compact Finite Difference Schemes with Spectral-Like Resolution," *Journal of Computational Physics*, Vol. 103, No. 1, 1992, pp. 16–42.

[19] Colonius, T., Lele, S. K., and Moin, P., "Boundary Conditions for Direct Computation of Aerodynamic Sound Generation," *AIAA Journal*, Vol. 31, No. 9, 1993, pp. 1174–1182.

M. Samimy
Associate Editor